JOURNAL OF MATERIALS SCIENCE 30 (1995) 6097–6104

Laser surface melting and alloying of type 304 L stainless steel

Part I *Microstructural characterization*

O. V. AKGUN, O. T. INAL*
Department of Materials and Metallurgical Engineering, New Mexico Institute of Mining and Technology, Socorro, NM 87801, USA

Microstructures of laser surface melted (LSM) and alloyed (molybdenum and tantalum) type 304L stainless steel have been studied. δ-ferrite was found to be the primary solidification phase for these alloys. Chemical analysis of the laser-processed layers indicated no compositional variation between the as-received and laser-processed layers in terms of major alloying elements, i.e. chromium and nickel. However, laser processing resulted in a lowered manganese content, by about 15%. Furthermore, TEM studies showed laser processing to introduce extensive amorphous Mn–Si precipitation into the microstructure.

1. Introduction

Surface features, such as grain size, defects, macro/micro compositional variations, and residual stresses determine corrosion, fatigue, and wear properties of most materials. Because it is frequently too difficult or expensive to optimize all these properties in the entire volume of a product, surface modification techniques provide an alternative for the enhancement of surface properties.

In the last two decades, laser treatment of metals and alloys has emerged as a novel surface modification technique [1–5]. Consequently, laser-processing techniques, such as laser surface heating (LSH), laser surface melting (LSM), and laser surface alloying (LSA) have found wide engineering applications.

The purpose of the present study was to utilize laser surface modification techniques, namely LSM and LSA, to improve wear resistance of AISI 304 L stainless steel, without degrading the inherent corrosion-resistance properties. For this purpose, molybdenum and tantalum were the alloying elements used in this study. This paper details LSM and LSA (molybdenum and tantalum) of type 304 L austenitic stainless steel and the associated microstructural changes that emanate from these treatments.

2. Experimental procedure

2.1. Laser source

A GTE Sylvania Model 975 CO_2 continuous wave (CW) gas-transport laser, which provides a nominal output power of 5000 W continuous infrared radiation at a wavelength of 10.6 μm, was used in this study. The test specimens were mounted on a unidirectional table, scanned with a focused beam, 0.5 mm diameter, at a speed of 7 mm s^{-1} and protected during the processing by flowing argon gas for surface-alloyed samples, or nitrogen gas for surface melting. The total sample surface area of 19.3 cm^2 was melted with 50% overlap.

2.2. Materials

The substrate material used in this study was AISI 304 L austenitic stainless steel. Chemical composition and mechanical properties of AISI 304 L are given in Table I. The as-received bar was cut to sizes of 5.08 cm × 3.81 cm × 1.27 cm plates. They were polished with 600 grit SiC paper and cleaned with methanol in an ultrasonic cleaner before laser treatment.

2.3. Alloying

Alloying elements used in this study were in the form of commercial thin foils of 99.95% purity and a thickness of 0.025 mm. The alloying process was performed

TABLE I (a) Chemical composition and (b) mechanical properties[a] of as-received AISI 304 L stainless steel

(a)

C	Mn	Si	S	P	Cr	Ni	Mo
0.017	1.64	0.55	0.027	0.22	18.22	8.18	0.40
Co	Cu	Ti	N	Cb, Ta	Fe		
0.22	0.22	< 0.02	0.08	0.06	Bal.		

(b)

UTS (MPa)	0.2%YS (MPa)	%EL (in)	%RA	BHN
609	268.2	63.6	78.8	143/156

[a] Annealed 1065 °C, 20 min and water quenched.

* Author to whom all correspondence should be addressed.

0022–2461

in two steps; first, a thin foil placed on the substrate was irradiated with low power (2.5 kW) and 0% overlap. This step gave efficient alloying. In the second step, the sample was rotated 90° about the short axis, with the laser beam still perpendicular to the previously treated surface, scanned with high laser power (5 kW) and 50% overlap. As a result of the second step, a more uniform compositional distribution in the alloyed layer was achieved.

2.4. Chemical analysis

The compositions of the samples, after laser surface melting and alloying, were determined by inductively coupled plasma–atomic emission spectroscopy (ICP–AES) at Sandia National Laboratory, Albuquerque, NM.

2.5. Optical microscopy

A Unitron Versamet-2 optical microscope was used for microstructural characterization after laser surface melting or alloying. After laser treatment, specimens were polished with 0.05 μm alumina and etched with a solution of 10 ml HCl, 20 ml HNO_3 and 30 ml H_2O; this etchant makes δ-ferrite appear to be dark.

2.6. X-ray diffraction (XRD)

A Philips Diffractometer Model PN 1720 X-ray generator was utilized to determine the phase changes that incurred following laser surface melting and alloying. CuK_α radiation was used as the X-ray source. Standard polishing and cleaning procedures were followed for the XRD samples. Phase compositions were determined from the XRD data. For these calculations, it was assumed that preferred orientation introduced in laser melting would not affect the amount of the phases present, elucidated in the melted layer. The sharp shape of the diffraction peaks obtained from the laser-treated surfaces indicates that residual stresses are absent in the treated layers (12) (see Fig. 7 below for the LSM sample). Lattice parameters of the samples were measured by the Debye–Scherrer powder method. The samples, sectioned parallel to the surface of treatment, were thinned to a few micrometres thickness. They were then cut into small pieces and placed in a silicon tube for this scrutiny. An extrapolated method was used to determine the lattice parameters. To minimize errors, high-angle diffraction lines were selected for the measurements. Lattice constant, a_0 versus $1/2\ [(\cos^2\theta/\sin\theta) + (\cos^2\theta/\theta)]$ (extrapolation function) were plotted and the a_0 values were determined for the samples.

2.7. Transmission electron microscopy

A Jeol-100C electron microscope, operated at 100 kV, was used to evaluate microstructural differences between the laser-surface-melted and alloyed type 304 L austenitic stainless steel samples. Thin foils were prepared from the mid-region of the melted or alloyed layer. Disc specimens of 3 mm diameter were punched and further thinned by electropolishing in a solution of 10% perchloric acid and 90% methanol with a twin jet polisher at 50 V, 80 mA, and at room temperature.

X-ray microanalysis was performed at the University of New Mexico, Geology Department, analytical electron microscope (AEM) facilities. A Jeol-2000FX, operated at 200 kV, equipped with a Tracor Northern energy dispersive spectrometer (EDS), was used.

3. Results and discussion

3.1. Laser-surface-melted 304 L

Fig. 1 shows the LSM layer that has a melt depth of 800 μm. As shown in Fig. 2, regrowth occurred epitaxially from the grains of the substrate into the fusion zone. Solidification structure at maximum depth is a plane-front of a few micrometres, and this converts, towards the surface, to a columnar dendritic structure. 304 L austenitic stainless steel does not transform to martensite following laser melting [6] and thus the

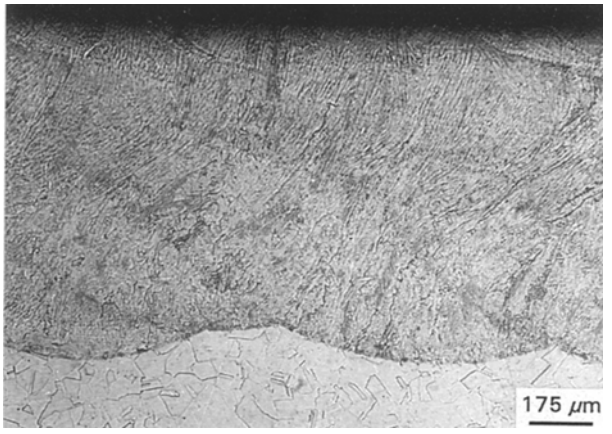

Figure 1 Optical micrograph of LSM type 304 L.

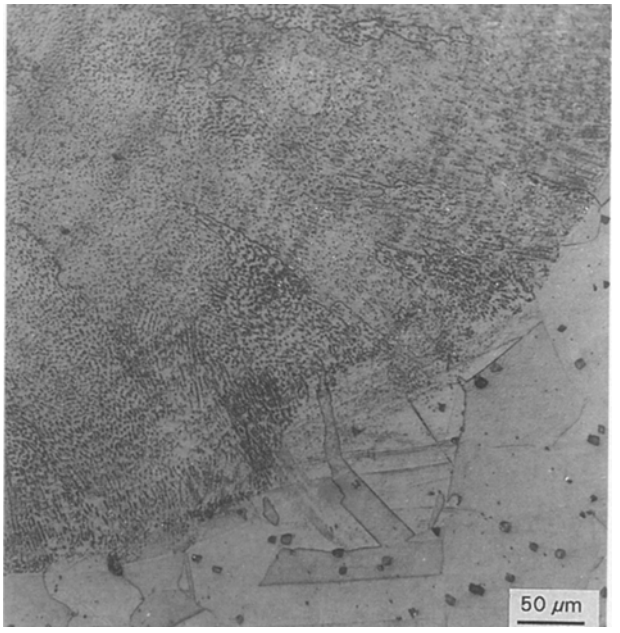

Figure 2 Expitaxial regrowth from the substrate of LSM type 304 L.

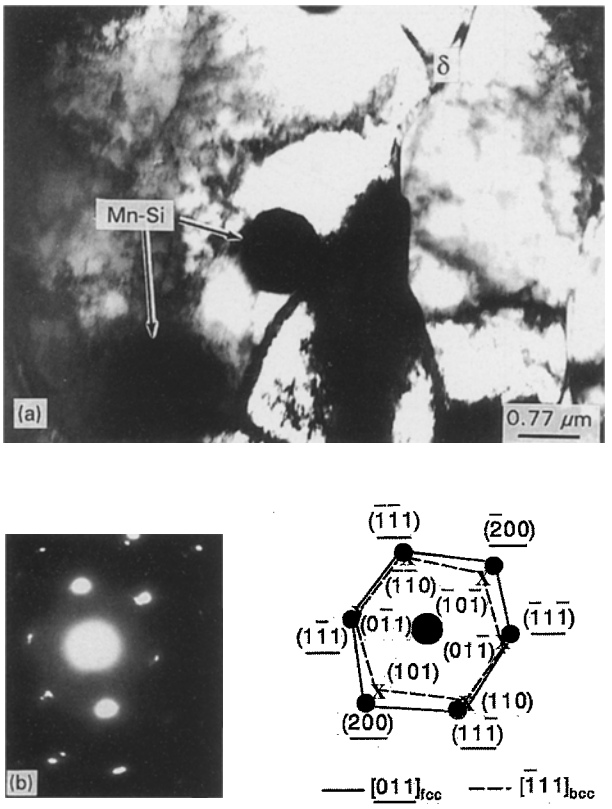

Figure 3 Transmission electron micrograph of LSM type 304 L: (a) bright-field image showing δ-ferrite and Mn–Si particles; (b) diffraction pattern.

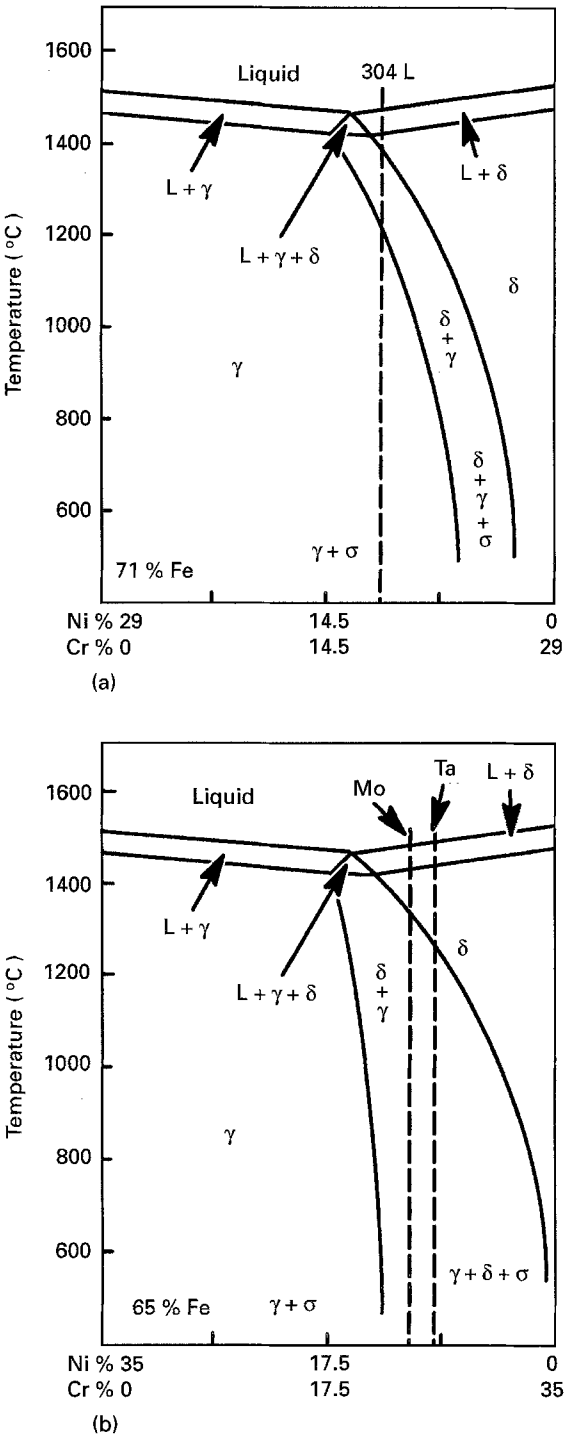

Figure 4 Fe–Cr–Ni pseudo-binary phase diagrams of (a) LSM, (b) molybdenum- and tantalum-alloyed type 304 L.

only microstructural changes that are presently observed after laser melting are a reduction in subgrain size and a duplex structure of γ- and δ-ferrite (the latter being finely dispersed in the former).

Fig. 3 shows a transmission electron micrograph of LSM 304 L microstructure containing γ- and δ-ferrite. An interesting observation from the micrographs of the laser-processed samples is the presence of perfectly spherical particles. AEM/EDS analysis indicates that they consist of manganese and silicon, and diffraction patterns also confirm their amorphous structure. Vitek *et al.* [7] and David *et al.* [8] first reported the presence of these particles in laser-welded 308 and 316A austenitic stainless steels, and they also showed that these particles were amorphous Mn–Si. They attributed their formation to preferential evaporation of manganese and silicon and later recondensing of these on the wall of the keyhole formed during laser melting. In this study, LSM and LSA were not performed in the keyhole regime. This suggests that the formation of these Mn–Si precipitates is independent of keyhole formation.

Fig. 4 shows the approximate composition of the alloys studied superimposed on the Fe–Cr–Ni pseudo-binary phase diagram. All alloy compositions fall on the primary ferrite side of the eutectic triangle. In this study, the primary solidification mode for the samples was determined from a thermodynamic model using chromium and nickel equivalents (Cr_{eq} and Ni_{eq}) [9]. This model calculates the massive solidification temperature, T_0, for each phase, γ- and δ-ferrite, and assumes that the primary solidification phase is the one that has a higher T_0 temperature; then, solidification starts from that temperature. Fig. 5 shows the calculated thermal stability of the phases for the samples. As seen in Fig. 5, δ-ferrite is the primary solidification phase for the alloy compositions studied.

The cooling rate for LSM samples was calculated from secondary dendritic arm spacing [10] to be of the order of 10^4–10^5 °C s^{-1}. Because the solidification mode for 304 L at this cooling rate is primary δ-ferrite, rapid solidification retained this high-temperature phase at room temperature. The volume fraction of δ-ferrite was calculated to be 4.3 vol % at the surface

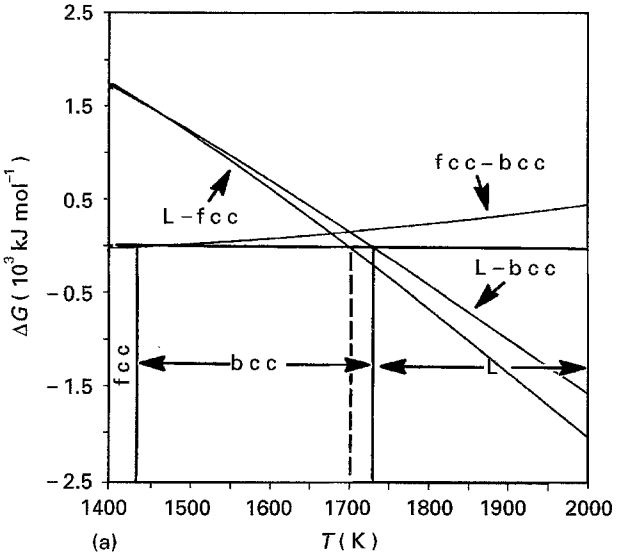

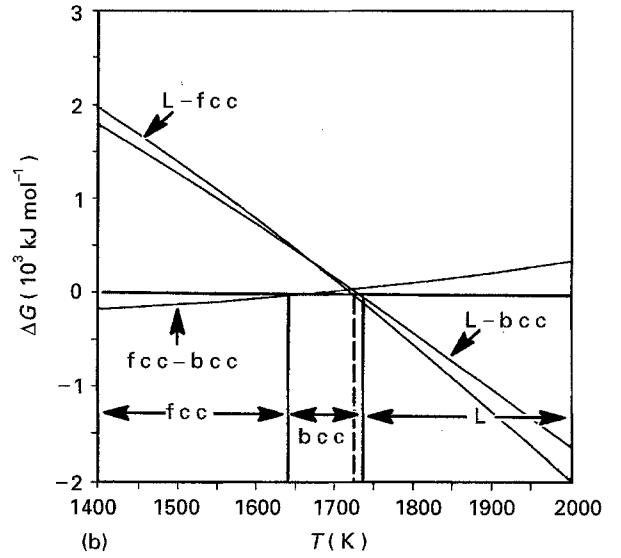

Figure 5 Thermal stability of phases in (a) LSA and (b) LSM samples. (For LSA samples it is assumed both have the same Cr_{eq}). (---) Metastable austenite solidification temperature.

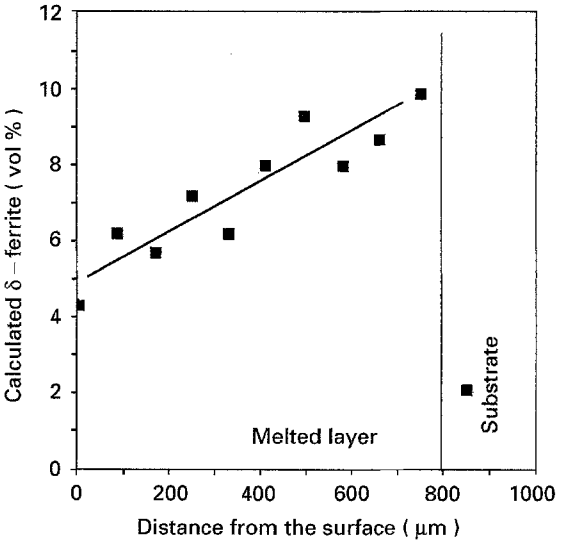

Figure 6 δ-ferrite profile in the melted layer.

from the X-ray data shown in Table II. The solidification sequence for LSM samples then becomes different from that shown in Fig. 4a, L → L + δ → δ + γ → γ + δ (untransformed).

It is important to realize that the melted layer experiences different cooling rates at different depths during solidification, due to the heat-transfer characteristics of the substrate and its surrounding environment, i.e. the shielding gas. Cooling rate is directly related to the dissipation rate of heat input. Thermal properties of the substrate are very important for heat dissipation. For example, 304 L stainless steel has very poor thermal conductivity, 0.168 (compared with copper, 4.01) Watt $cm^{-1}\,°C^{-1}$ and diffusivity, 0.0538 (compared with copper, 1.1403) $cm^2\,s^{-1}$. Heat input, on the other hand, for the case of laser melting is a function of power density, scan speed, and absorptivity of the substrate or the treated surface. Higher power density, low scan speed, and high absorptivity cause more heat input into the material.

Cooling rate seems to have a very significant effect on retained δ-ferrite content. XRD, taken from the surface of the melted layer and after successive removals of 50 μm thicknesses at a time, indicates that the volume fraction of δ-ferrite in the melted layer increases constantly towards the boundary between the melted zone and the substrate, where it reaches 9.9 vol % (Fig. 6). δ-ferrite gradients, observed here for LSM, have been reported by Mignone *et al.* [11] and La Barbera *et al.* [12] for the electron-beam-melted 304 stainless steel.

The effect of shielding gas on the retained δ-ferrite content has been studied in the welding of 304 L stainless steel [13, 14]. δ-ferrite content has been reported to decrease with an increase in nitrogen content of the shielding gas, i.e. Ar + $x\%N_2$. We performed two LSM studies on type 304 L: one with 100% nitrogen gas and another with 100% argon. XRD results indicate δ-ferrite content to be the same for both cases (Fig. 7). It is clear that for this particular case, other factors, such as heat input or scan speed, may have more influence on the δ-ferrite content than the type of shielding gas used.

The effects of LSM at constant power, 5 kW, and varying scan speed, on final resolidified structure, are schematically shown in Fig. 8. In the case of high scan speed (Fig. 8a), melt depth is very shallow, i.e. 20–50 μm, which means that only a few grains were melted. Because dendritic growth follows substrate grain direction, dendrites can reach the surface with no or minimum disruption by their neighbours, thus resulting in a more uniformly oriented structure.

TABLE II XRD of LSM type 304 L

I/I_0	2θ (deg)	*d*-spacing (nm)	Identification
100	43.600	2.079	γ (1 1 1)
28	74.671	1.271	γ (2 2 0)
26	50.733	1.798	γ (2 0 0)
17	90.594	1.084	γ (1 1 3)
8	95.910	1.038	γ (2 2 2)
6	44.575	2.033	δ (1 1 0)

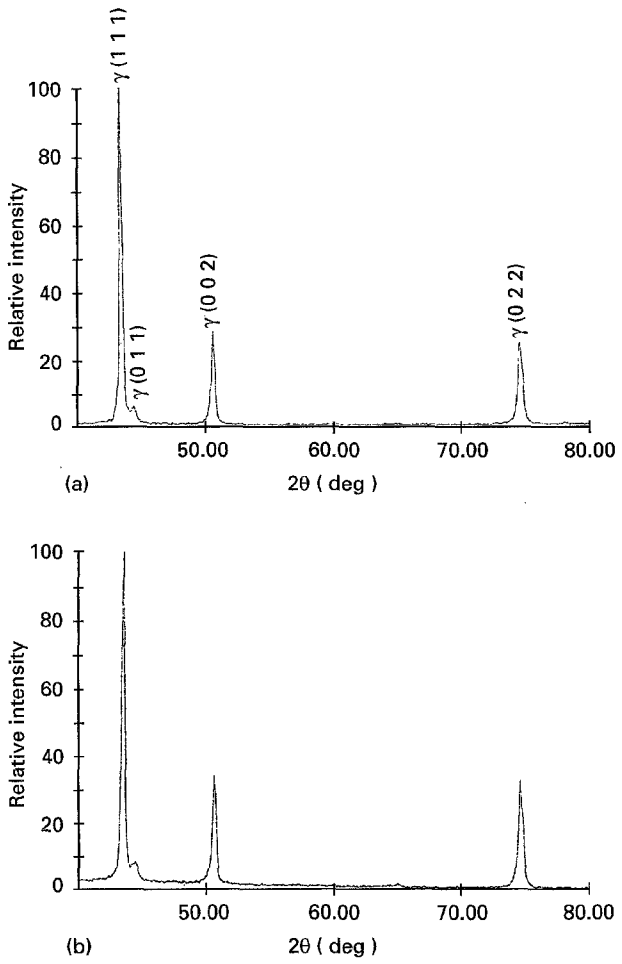

Figure 7 XRD of LSM 304 L under (a) nitrogen, and (b) argon gas.

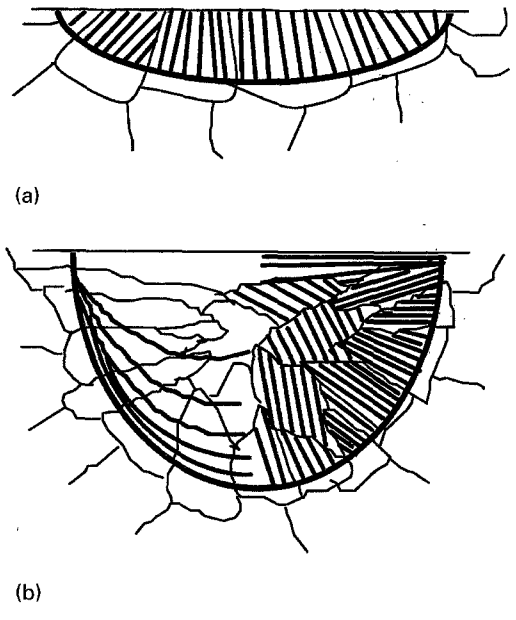

Figure 8 Change in microstructure of the single melt path of type 304 L at (a) high (×100) and (b) low (×40) scan speeds.

The situation changes as melt depth increases, at low scan speed; this is because of the fact that more grains will be involved in the melting process (Fig. 8b). Then, dendrites will grow from the grains that have different orientations leading to more disruption by their neighbours. Thus the degree of orientation uniformity in the resolidified structure will decrease.

Another characteristic feature, observed in the deep-melted structure, is lines that are almost parallel to the boundary between the melted zone and the substrate, and are stacked closely at the bottom and separated with increasing distances toward the centre of the resolidified structure (left part of Fig. 8b). The nature of these lines, called banding, was not investigated. In general, there are a number of reasons for banding to occur in a weld [15]. Some of these are process related, such as fluctuations in the welding speed and power, fluctuations in the weld pool due to shielding gas, and magnetic or gravitational forces. In the final analysis, all these parameters affect the cooling rate in the weld pool. Because the bands appeared in the LSM material with high melt depth, they are believed to be a result of changing cooling rates in the molten pool having led to solute segregation.

Lattice parameters of austenite and δ-ferrite phases were determined, and the lattice parameter of austenite was found to be 0.12% smaller than that of the as-received sample (Table III). It is assumed that this difference is related to the nature of laser processing. The highly focused heat of the laser beam could remove some carbon and nitrogen. The presence of these elements has a stronger effect for distortion of the austenite lattice than other alloying elements. Even though LSM does not introduce any compositional change to the melted layer in terms of major alloying elements, i.e. iron, chromium and nickel, in 304 stainless steel (see Table IV) [16–18], what happens to the carbon and nitrogen content after LSM is not known and has not been investigated in detail. On the other hand, Auger electron spectroscopy data obtained by McCafferty and Moore for laser-surface-melted and as-received 304 stainless steels indicate almost 50% reduction in carbon content for laser-treated 304 stainless steel [17]. Their analysis clearly supports our explanation for the decreased lattice parameter of the γ-phase observed in this study.

TABLE III Microstructure summary of the samples

Alloy[a]	Thickness (μm)	Phases (vol %)	Lattice parameter (nm)
AR	–	Austenite (98%)	0.360 13
		δ-ferrite (2%)	0.288 93
LSM	800	Austenite (96%)	0.359 69
		δ-ferrite (4%)	0.28 75
LSA-Mo	500	Austenite (23%)	0.361 49
		δ-ferrite (77%)	0.288 53
LSA-Ta	500	Austenite (24%)	0.360 88
		δ-ferrite (76%)	0.288 32

[a] AR, as-received; LSM; laser surface melting; LSA; laser surface alloying.

TABLE IV Compositions of the samples (wt %)

Sample	Ni	Cr	Mn	Si	Cu	Co	Mo	Ta	V
AR (av.)	8.00	17.7	1.57	0.66	0.23	0.20	0.35	< 0.01	0.15
(S.D.) ±	0.07	0.1	0.01	0.01	0.01	0.00	0.00	0.00	0.00
LSM (av.)	8.25	17.8	1.33	0.50	0.23	0.20	0.35	< 0.01	0.15
(S.D.) ±	0.15	0.5	0.11	0.06	0.01	0.00	0.01	0.00	0.01
Mo-alloyed									
(av.)	8.04	17.5	1.43	0.63	0.23	0.20	4.33	< 0.01	0.15
(S.D) ±	0.07	0.2	0.01	0.01	0.01	0.00	0.05	0.00	0.00
Ta-alloyed									
(av.)	7.89	17.1	1.32	0.62	0.23	0.20	0.35	6.84	0.15
(S.D.) ±	0.14	0.3	0.02	0.02	0.01	0.00	0.00	0.05	0.00

The results of chemical analysis of LSM and LSA materials are given in Table IV. The amounts of all major alloying elements are very close to those of the as-received material, except for manganese. Its content is around 15% less for the laser-processed materials than for the as-received ones. A lowered manganese content, around 25 wt %, in laser-welded AISI 202 stainless steel, was also reported by Khan *et al.* [19, 20]; this was attributed to the higher vaporization rate of manganese.

TABLE V XRD of LS molybdenum-alloyed type 304 L

I/I_0	2θ (deg)	*d*-spacing (nm)	Identification
100	44.384	2.040	δ (1 1 0)
40	81.782	1.178	δ (1 1 2)
22	43.339	2.087	γ (1 1 1)
9	64.563	1.443	δ (0 0 2)
9	74.265	1.278	γ (0 2 2)
7	50.443	1.807	γ (0 0 2)

3.2. Laser-surface-molybdenum-alloyed 304 L

A molybdenum-alloyed layer, 500 μm thick, is shown in Fig. 9. Based on the compositions given in Table IV, Cr_{eq} and Ni_{eq} were calculated to be 22.8 and 9.27 wt %, respectively. This gives a Cr_{eq} to Ni_{eq} ratio of 2.45 and indicates a primary δ-ferrite solidification mode for this alloy. This is shown in Fig. 4b. Solidification follows $L \rightarrow L + \delta \rightarrow \delta + \gamma$; this solidification sequence is revealed in the XRD data (Table V). The amount of δ-ferrite was also calculated from XRD to be 77 vol%. The higher equivalent ratio and cooling rate in this case promote a higher δ-ferrite and lower austenite content to exist at room temperature. The δ-ferrite morphology is observed to be arranged in a parallel-sided, plate-like structure, and Mn–Si particles are present in the microstructure as well (Fig. 10).

Lattice parameters of austenite and ferrite phases were determined to be 0.361 49 and 0.288 53 nm, respectively

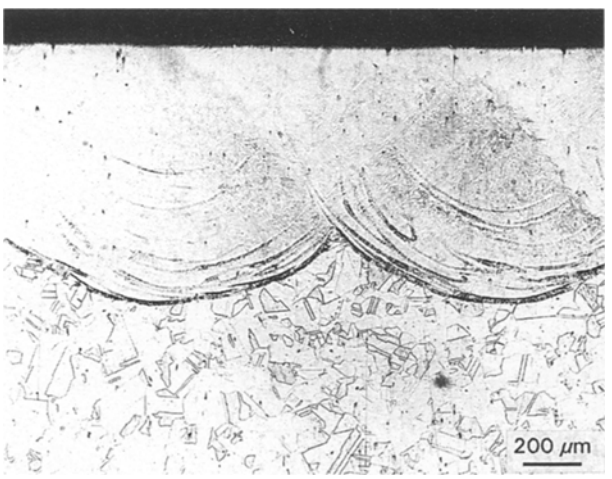

Figure 9 Optical micrograph of LS molybdenum-alloyed type 304 L.

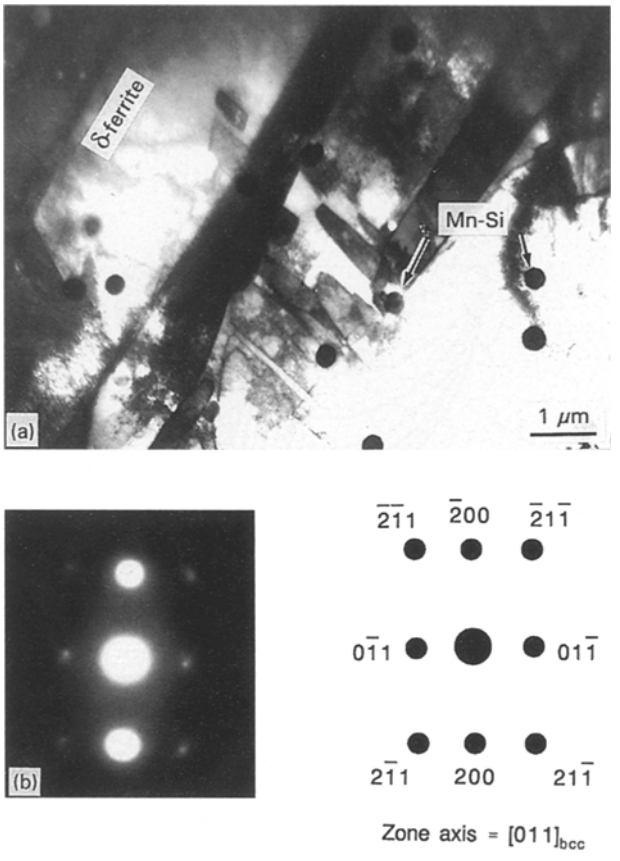

Figure 10 Transmission electron micrograph of LS molybdenum-alloyed type 304 L: (a) bright-field image showing δ-ferrite plates and Mn–Si particles, (b) diffraction pattern.

(Table III). This difference in austenite lattice constant as compared to LSM emanates from the fact that molybdenum has a favourable atomic size factor for substitutional solid solution in the austenite phase. An increase in δ-ferrite lattice constant as compared to LSM is also due to higher molybdenum solubility in the γ-phase.

3.3. Laser-surface-tantalum-alloyed 304 L

Fig. 11a shows the transverse section of a tantalum-alloyed layer that has a thickness of 500 μm. Micrographs taken parallel to the substrate from the upper surface (Fig. 11b) and at maximum melt depth (Fig. 11c) reveal some degree of tantalum segregation (grey etched region). This becomes clearer at the maximum melt depth (Fig. 11c). The most credible explanation of this is the higher density of tantalum, twice that of 304 L stainless steel (16.6 compared to 8 $g\,cm^{-3}$). During the alloying process, convection takes place in the melt pool and, because of higher density of tantalum or tantalum-containing phases, they could be deposited at the maximum melt depth.

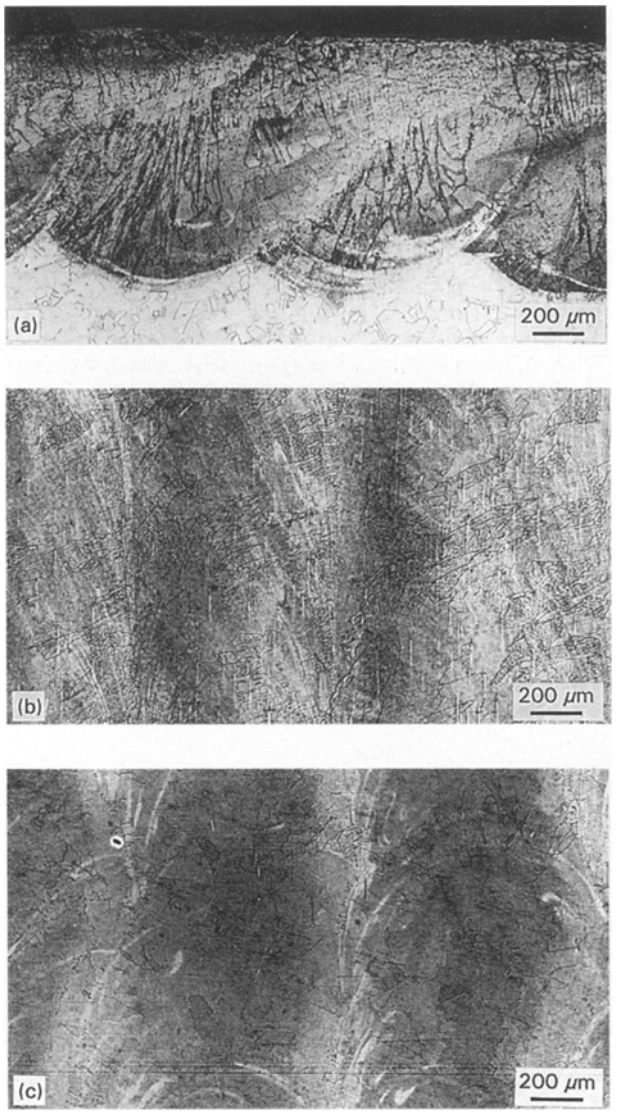

Figure 11 Optical micrograph of LS tantalum-alloyed type 304 L (a), (b) from the surface, and (c) maximum melt depth.

TABLE VI XRD of LS-tantalum-alloyed type 304 L

I/I_0	2θ (deg)	d-spacing (nm)	Identification
100	44.391	2.039	δ (1 1 0)
38	81.927	1.177	δ (1 1 2)
28	64.606	1.442	δ (0 0 2)
23	43.441	2.084	γ (1 1 1)
10	50.538	1.804	γ (0 0 2)
9	74.515	1.276	γ (0 2 2)
6	41.731	2.164	Unknown
5	38.334	2.348	Unknown

XRD data indicate that δ-ferrite has the highest intensities, followed by the austenite phase (Table VI), strongly confirming the ferrite-stabilizing effect of tantalum. The solidification path is also similar to that of molybdenum-alloyed material, as also confirmed by the XRD data (Table VI). Because of this higher equivalent ratio and the high cooling rate, the δ-ferrite content is 76 vol % at room temperature. TEM (Fig. 12) demonstrates that δ-ferrite is almost in a semi-continuous network structure, and some precipitates are seen as well as Mn–Si particles. It is believed that these precipitates are tantalum-based.

Lattice parameters of austenite and δ-ferrite phases were found to change by 0.33% and 0.28%, respectively, larger values than those for laser-surface-melted samples (Table III). Tantalum solubility in austenite and δ-ferrite phases are 2.9 wt % at 1215 °C and 7.7 wt % at 1442 °C, respectively. Tantalum solubility

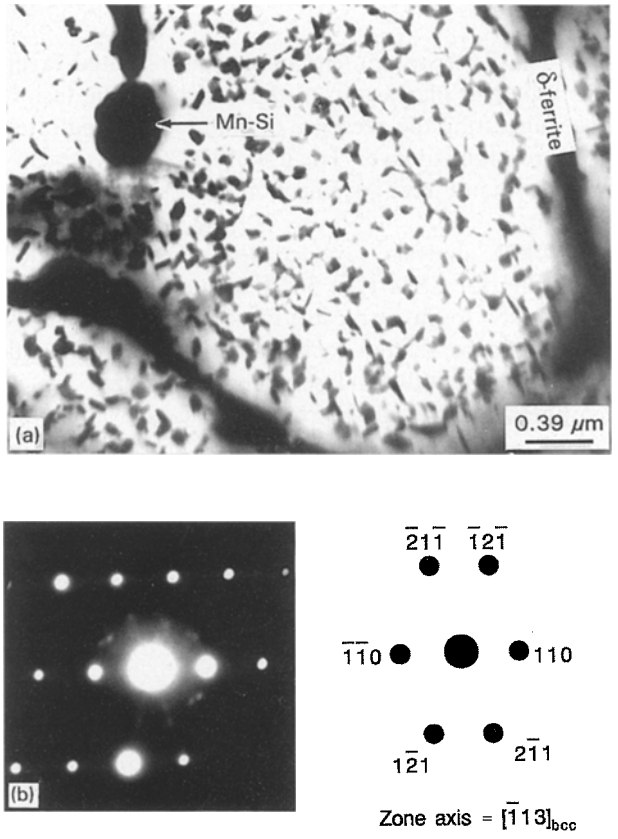

Figure 12 Transmission electron micrograph of LS tantalum-alloyed type 304 L: (a) bright-field image showing a semi-continuous network of δ-ferrite and Mn–Si particles; (b) diffraction pattern.

in these phases decreases with temperature. The amount of tantalum in the alloyed layer is close to 7 wt % (Table IV); for this reason the origin of the precipitates observed in the microstructure (Fig. 12) are assumed to be tantalum-based.

Chromium and nickel equivalents were calculated from Table IV to be 25.2 and 9.06, respectively. The ratio is 2.78 and confirms this alloy to solidify as primary δ-ferrite. The difficulty in calculating Cr_{eq} for tantalum is that there are no equivalents that include tantalum. Thus, the calculation assumes here that the constant in front of the weight percentage was one. On the other hand, the calculated δ-ferrite contents for molybdenum- and tantalum-alloyed samples are the same; from this information, the constant for tantalum could be predicted. To determine Cr_{eq} for the tantalum-alloyed sample, it can be assumed that tantalum-alloyed material has the same Cr_{eq}/Ni_{eq} ratio as the molybdenum alloyed material; this assumption is justified from the δ-ferrite content of both samples. From the new value of Cr_{eq}, and Schaeffler equivalents [21], the constant is calculated to be 0.56. This indicates a smaller ferrite-stabilizing effect for tantalum as compared to molybdenum.

4. Conclusions

1. δ-ferrite is the primary solidification phase for LSM and LSA samples. The δ-ferrite content is less than 10 and 80 vol % for LSM and LSA (molybdenum and tantalum) samples, respectively.

2. The solidification paths for the samples are $L \rightarrow L + \delta \rightarrow \gamma + \delta$ (minor phase) and $L \rightarrow L + \delta \rightarrow \delta + \gamma$ (minor phase) for LSM and LSA samples, respectively.

3. The δ-ferrite content in the laser-melted layer was found to increase from the surface to the fusion line, suggesting the presence of different cooling rates in the resolidified layer. The use of 100% N_2 as shielding gas did not have any effect on the retained δ-ferrite content.

4. XRD analysis revealed that austenite lattice parameter for LSM type 304 L samples decreased in comparison to the as-received 304 L substrate. This is believed to be related to the change in carbon and nitrogen content due to laser melting. Austenite lattice parameters showed an increase for the case of molybdenum and tantalum-alloyed samples. These increases are due to the substitutional solid solution of molybdenum and tantalum in the austenite phase.

5. Heavy precipitation of amorphous Mn–Si was observed for all laser-processed samples, even without keyhole formation. The manganese content was found to be lowered for all laser-processed samples as compared to as-received alloy. Both lowered manganese content and Mn–Si formation are characteristic features for laser surface melted and alloyed samples.

Acknowledgement

The support of this study by EPRI under contract RP2426-39 is gratefully acknowledged.

References

1. F. D. SEEMAN and D. S. GNANAMUTHU, *Metal. Prog.* **118** (1975) 67.
2. E. M. BREINAN, B. H. KEAR and C. M. BANAS, *Phys. Today* **29** (1976) 44.
3. C. W. DRAPER, *J. Metals* **35** (1982) 24.
4. B. R. APPLETON, B. SARTWELL, P. S. PEERCY, R. SCHAEFER and R. OSGOOD, *Mater. Sci. Eng.* **70** (1985) 23.
5. E. McCAFFERTY, G. K. HUBLER, P. M. NATISHAN, P. G. MOORE, R. A. KANT and B. D. SARTWELL, *ibid.* **86** (1987) 1.
6. O. V. AKGUN and O. T. INAL, *J. Mater. Sci. Eng.* **27** (1992) 2147.
7. J. M. VITEK, A. DASGUPTA and S. A. DAVID, *Metall. Trans.* **14A** (1983) 1833.
8. S. A. DAVID, J. M. VITEK and T. L. HEBBLE, *Weld. J.* **66** (1987) 289s.
9. K. OZBAYSAL, PhD dissertation, New Mexico Tech (1989).
10. N. J. NICHOLSAN, *J. Metals.* **31** (1983) 20.
11. A. MIGNONE, A. LA BARBERA, S. MARTELLI, M. VITTORI and R. FESTA, in "Corrosion behavior of duplex steel obtained by electron beam treatment of AISI 304", 10th International Conference Metal Corrosion (DGM Informationsgesellshaft, Oberursel, 1980) p. 1773.
12. A. LA BARBERA, S. MARTELLI, A. MIGNONE, F. PIERDOMINICI, M. VITTORI and G. LULLI, in Proceedings of the European Conference on "Laser Treatment of Materials", edited by Barry L. Mordike (1986) p. 179.
13. W. R. CIESLAK, D. J. DUQUETTE and W. F. SAVAGE, in "Trends in welding research in the United States", edited by S. A. David (American Society for Metals, Metals Park, OH (1982) p. 361.
14. U. KAMACHI MUDALI, R. K. DOYAL, T. P. S. GILL and J. B. GNANAMOORTHY, *Corrosion* **46** (1990) 454.
15. S. KOU, "Welding metallurgy" (Wiley, New York, 1987) pp. 137, 201.
16. J. DE DAMBORENA, A. J. VAZQUEZ, J. A. GONZALEZ and D. R.F. WEST, *Surf. Eng.* **5** (1989) 235.
17. E. McCAFFERTY and P. G. MOORE, *J. Electrochem. Soc.* **133** (1986) 1090.
18. J. STEWART, D. B. WELLS, P. M. SCOTT and A. S. BRANSDEN, *Corrosion* **46** (1990) 618.
19. P. A. A. KHAN and T. DEBROY, *Weld. J.* **67** (1988) 1s.
21. A. L. SCHAEFFLER, *Metal. Progr.* **56** (1949) 689.

Received 4 January 1994
and accepted 7 June 1995